

THE INFLUENCE OF THE TURBULENT/NON-TURBULENT INTERFACE GEOMETRY ON LOCAL ENTRAINMENT

Dhiren Mistry

Dep. of Energy and Process Engineering
NTNU
Trondheim N-7491, Norway
dhiren.v.mistry@ntnu.no

James R. Dawson

Dep. of Energy and Process Engineering
NTNU
Trondheim N-7491, Norway
james.r.dawson@ntnu.no

Jimmy Philip

Department of Mechanical Engineering
The University of Melbourne
Parkville, VIC 3010, Australia
jimmyp@unimelb.edu.au

Ivan Marusic

Department of Mechanical Engineering
The University of Melbourne
Parkville, VIC 3010, Australia
imarusic@unimelb.edu.au

ABSTRACT

In this paper we examine the local entrainment velocity (v_n) along the turbulent/non-turbulent interface (TNTI) to determine how v_n is influenced by the local geometry of the TNTI. Time-resolved, simultaneous particle image velocimetry (PIV) and planar laser-induced fluorescence (PLIF) measurements were taken in the far-field of an axisymmetric jet at $Re = 25\,300$. We use isocontours of scalar concentration ($Sc \gg 1$) to identify the TNTI and implement an interface-tracking technique to determine the local entrainment velocity along the TNTI. The TNTI geometry is characterised using (i) the interface radial position, (ii) the local interface curvature and (iii) the orientation of the TNTI surface. We evaluate the conditional v_n characteristics as a function of these three features. There is greater local entrainment when the TNTI is near to the centreline of the jet and in regions of convex curvature. We also consider the interface-normal fluid velocity about the TNTI to understand how the surrounding flow-field shapes these geometric features and influences the local entrainment. There is greater inflow of non-turbulent fluid towards the TNTI when the interface is nearer to the jet centreline and along convex curvatures, which hints at the presence of a turbulent structure that is common to positive local entrainment events along the TNTI.

INTRODUCTION

Local entrainment in turbulent flows is defined as the transport of unmixed or irrotational fluid across the boundary between the turbulent and non-turbulent fluid: the turbulent/non-turbulent interface (TNTI). Positive entrainment means that irrotational fluid adjacent to the TNTI acquires vorticity, which gives rise to a mass flux of fluid into the turbulent region of the flow. In a similar manner, detrainment refers to the mass flux of fluid from the turbulent region into the non-turbulent region. The process of entrainment is prevalent in a range of scientific and engineering flow scenarios, such as the smoke emitted from a smokestack. In this example the local entrainment rate

along the TNTI will determine the local concentration of the pollutants in the surroundings. It is therefore of interest to understand the mechanisms that influence the entrainment rates along the TNTI.

Three-dimensional particle tracking measurements and DNS simulations on round and planar jets have shown that the entrainment velocity exhibits some dependency on the local TNTI geometry. For example, the local entrainment velocity exhibits some coupling to the local surface curvature Holzner & Lüthi (2011). Generally, the local entrainment velocity v_n is more negative (positive entrainment) along points where the TNTI curvature is convex, and v_n is more positive (detrainment) along points where the curvature is concave (Wolf *et al.*, 2012). There is also some dependence of v_n on the surface orientation of the TNTI (Watanabe *et al.*, 2014). However, it is not fully understood why these geometric features are coupled to local entrainment or if there are underlying turbulent structures that are common between these features. In this paper we investigate the dependence of the local entrainment rate on the radial distance from the jet centreline to the TNTI, the local surface curvature and the orientation of the TNTI. We then proceed to examine the flow-patterns about the TNTI that correspond to these geometric features, with the aim to link a common description of the flow kinematics with the local entrainment.

EXPERIMENTAL SETUP

The results presented in this paper are evaluated using simultaneous, time-resolved PIV/PLIF measurements of an axisymmetric jet in water. These measurements were performed in the streamwise-radial plane of the jet centred at $x/d = 50$, where $d = 10$ mm is the diameter of the nozzle. The Reynolds number of the jet at the nozzle-exit is $Re = 25\,300$, where $Re = U_e d / \nu$, $U_e = 2.53$ ms^{-1} is the nozzle exit velocity and $\nu = 1 \times 10^{-6}$ $\text{m}^2 \text{s}^{-1}$ is the kinematic viscosity. Additional details regarding the experimental set-up may be found in Mistry *et al.* (2016). A total of 32000 temporally-resolved vector fields were acquired,

but the analysis presented in this paper is calculated using 1080 instantaneous planar fields equally-spaced in time. The particle images were processed using DaVis 8.2 (LaVision GmbH) using 24 pixel interrogation windows and 75% window-overlap. The resultant PIV vector spacing is 10η ,

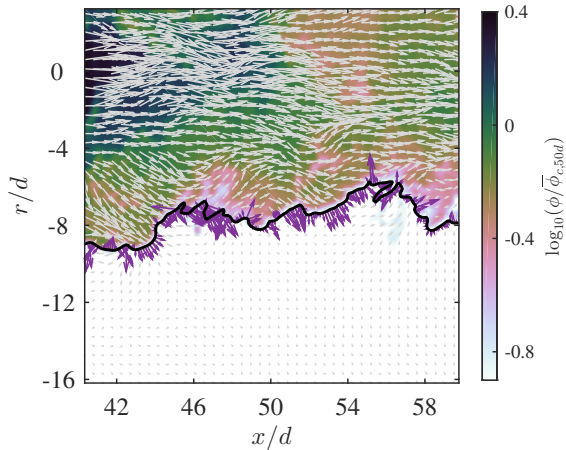


Figure 1. Example of the simultaneous velocity and scalar data. The scalar concentration field is shown in logarithmic scaling in the background, with the TNTI denoted by the black line. The instantaneous velocity vectors from the PIV camera are superimposed onto the figure in grey. Along the TNTI we plot the local entrainment velocity, \mathbf{V} , in purple. The length of the purple \mathbf{V} vectors and the grey velocity vectors are scaled differently.

TNTI identification

We use isocontours of the scalar concentration field, ϕ , as a surrogate for the TNTI. Passive scalars have been used previously in planar PIV/PLIF experiments on a jet by Westerweel *et al.* (2009) and has been shown by Gampert *et al.* (2014) (for $Sc = 1$) to agree very well with the 3D vorticity field in a DNS of a temporal mixing layer. Even with increasing Schmidt number (up to $Sc = 8$), Watanabe *et al.* (2015) report that the scalar boundary of a turbulent mixing layer still falls within the finite region of the TNTI. Thus, we are confident that $Sc \gg 1$ scalar isosurfaces coincide with the (vorticity) TNTI at the spatial resolution of our measurement. We implement an empirical process similar to that described by Prasad & Sreenivasan (1989) to identify the scalar concentration threshold value that best represents the TNTI. This scalar threshold is determined to be $\phi/\phi_c = 0.18$ (Mistry *et al.*, 2016), where ϕ_c is the local mean centreline scalar concentration, which is applied to each centreline-normalised, instantaneous scalar concentration field. The TNTI is extracted by applying the `contour` function in Matlab (MathWorks) and selecting the longest continuous isocontour. As shown by Mistry *et al.* (2016), there is a jump in the spanwise vorticity magnitude profile, $\langle |\omega_z| \rangle$, across the TNTI. This represents the transition of vorticity between the turbulent and non-turbulent levels. This indicates that the scalar isocontours defined by $\phi/\phi_c = 0.18$ do

indeed isolate the turbulent and non-turbulent regions of this jet flow. In this paper we ignore instances of “holes” in the turbulent region and “islands” in the non-turbulent region that arise from the planar slice through the 3D scalar concentration field. These features are neglected in the analysis presented here because the total area of these features is less than 1% of the total area of the measured turbulent region.

Measuring the local entrainment velocity

In this paper we use an interface-tracking technique to measure the entrainment or detrainment of the turbulent region along the TNTI. This is achieved by subtracting the contribution of the local fluid velocity (advection) from the overall motion of the TNTI; the remaining motion of the TNTI is attributed to the local entrainment. The high-speed PLIF measurements allows us to track the overall motion of the TNTI in time and the simultaneous high-speed PIV measurements allows us to interpolate the local fluid velocity (advection) along the TNTI at the same time. This process is similar to the “graphical” approach of Wolf *et al.* (2012) who measured the entrainment velocity using 3D particle tracking data in a turbulent jet.

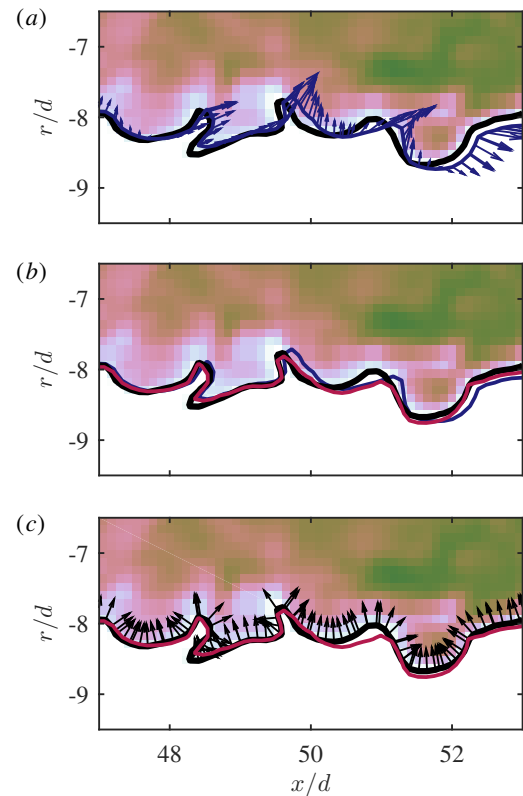


Figure 2. Schematics illustrating the measurement of the local entrainment velocity along the TNTI (see text for description).

Figure 2(a) illustrates the TNTI at an arbitrary time, t_0 . At a later time $t_0 + dt$ (panel b) the TNTI has moved because of the sum of the local flow advection and the local entrainment, $\mathbf{u}_s = \mathbf{u}_f + \mathbf{V}$. Because we have simultaneously measured the velocity field, we are able to subtract the effects of local advection (\mathbf{u}_f) by displacing the interface at

$t_0 + dt$ by distance $-\mathbf{u}_I dt$, where \mathbf{u}_I is the local fluid velocity interpolated along the interface using a bilinear interpolation scheme. The local entrainment velocity, $\mathbf{V} = v_n \mathbf{n}$, is finally measured by considering the local normal distance ($d\ell \mathbf{n}$) from the interface at t_0 to the advection-subtracted interface, $v_n = d\ell/dt$ (see panel *c*). The interface normals along the TNTI are pointing into the turbulent region, and therefore positive entrainment (*i.e.* a growing turbulent region) corresponds to a negative entrainment velocity, v_n .

To check the validity of the entrainment velocity measurement we compare the total mass-flux of the jet measured using a local and a global approach. From a local perspective, the mass-flux rate along the TNTI may be defined by the integral of the local entrainment velocity along the length of the TNTI:

$$\frac{d\Phi}{dx}^{\text{loc}} = \frac{1}{L_x} \int_0^{L_x} (-v_n) r_I ds. \quad (1)$$

Here a negative sign is added to the local entrainment velocity v_n because negative v_n corresponds with positive entrainment (*i.e.* spreading turbulent region). The overline denotes an ensemble average over the 1080 realisations of the flow, which gives the local mass-flux rate. We may similarly define the global mass-flux rate,

$$\frac{d\Phi}{dx}^{\text{glob}} = \frac{d}{dx} \left(\int_0^{\infty} \bar{u} r dr \right), \quad (2)$$

which considers the time-averaged axial velocity field \bar{u} that is integrated up to the upper and lower extents of the field-of-view of the PIV. We determine that the local mass-flux rate (1) is $\frac{d\Phi}{dx}^{\text{loc}} = 8.88 \times 10^{-4} \text{ m}^2 \text{ s}^{-1}$ and the global mass-flux rate (2) is $\frac{d\Phi}{dx}^{\text{glob}} = 8.20 \times 10^{-4} \text{ m}^2 \text{ s}^{-1}$. The excellent agreement (approximately 8% difference) between these mass-flux rates gives us confidence that the interface-tracking method described here accurately captures the local entrainment along the TNTI. The PDF of the entrainment velocity is presented in figure 3, which shows that the entrainment velocity is intermittent because of the wide tails and exhibits preference for positive entrainment (negative v_n) and therefore a growing turbulent region.

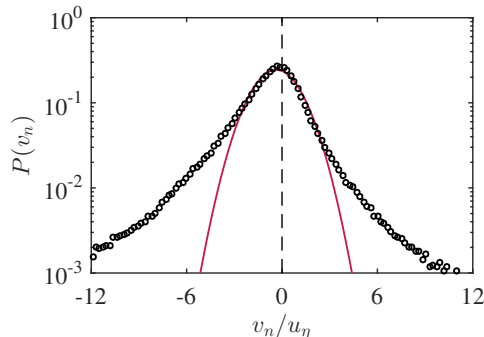


Figure 3. PDF of the entrainment velocity v_n measured along the TNTI for all 1080 realisations. A Gaussian profile fitted to the PDF is shown by the red line.

CHARACTERISTICS OF THE TNTI

In this section we characterise the geometry of the TNTI. In particular, we focus on the radial distance of the TNTI to the jet centreline, r_I , the interface curvature, κ , and the orientation of the TNTI, θ ; illustrations of these variables are presented in figure 4. The radial position of the interface, r_I , is the distance along the radial axis from the jet centreline to the local position of the TNTI (figure 4*d*). The interface curvature, κ , represents the rate of change of the interface direction (in two dimensions) and is evaluated using the following parametric expression:

$$\kappa = \frac{\frac{dx}{ds} \frac{d^2 r}{ds^2} - \frac{dr}{ds} \frac{d^2 x}{ds^2}}{\left[\left(\frac{dx}{ds} \right)^2 + \left(\frac{dr}{ds} \right)^2 \right]^{3/2}}. \quad (3)$$

Figure 4(*e*) illustrates the definition of convex ($\kappa > 0$) and concave ($\kappa < 0$) curvatures of the TNTI. The orientation of the TNTI, θ , is measured as the angle between the stream-wise axis, x , and the local interface-normal unit vector, \mathbf{n} . The angular range $90^\circ \leq \theta \leq 180^\circ$ represents the ‘leading edge’ of the interface, and $0^\circ \leq \theta < 90^\circ$ represents the ‘trailing edge’. Examples of the TNTI leading edge (L.E.) and trailing edge (T.E.) are highlighted in figure 4(*f*).

Figure 5 illustrates the PDFs of the three TNTI characteristics that we examine in this paper. The distribution of the TNTI radial position (r_I , panel *a*) agrees well with the fitted Gaussian line shown in red. This Gaussian behaviour is also observed for the TNTI in a range of free-shear flows (Westerweel *et al.*, 2009; Chauhan *et al.*, 2014; Watanabe *et al.*, 2014; Borrell & Jiménez, 2016). The two-dimensional curvature of the interface exhibits very wide tails (panel *b*), which is indicative of very sharp contortions. A very large and contorted surface area is necessary to balance the slow rate of diffusion across the interface (de Silva *et al.*, 2013). The PDF of the interface orientation (θ , panel *c*) demonstrates that the TNTI is not preferentially aligned to the jet axis. Note that in this plot an interface that is parallel to the jet centreline occurs at $\theta = 90^\circ$.

INFLUENCES ON LOCAL ENTRAINMENT

Given the TNTI geometric features identified in the previous section, we now evaluate the dependence of the local entrainment velocity on these geometric features. This is achieved by calculating the joint-probability density function (J-PDF) between the local entrainment velocity v_n and one of the geometric features of the TNTI that was as shown in figure 4(*d-f*). The J-PDFs are presented in figure 6, which shows the joint distributions of v_n and (*a*) radial distance to the TNTI r_I , (*b*) curvature κ and (*c*) interface orientation θ . Given some value of the independent variables (*i.e.* geometric feature), we also evaluate the conditional mean entrainment velocity $\bar{v}_n|_f$, where f represents r_I , κ or θ ; this is illustrated by the solid red lines in figure 6.

Figure 6(*a*) demonstrates that there is preference for greater entrainment (negative v_n) when the TNTI is nearer to the jet centreline (smaller r_I). This behaviour is illustrated by the conditional mean entrainment velocity $\bar{v}_n|_{r_I}$ shown by the red line. When the TNTI is far from the centreline ($r_I/b_{u,1/2} > 2.5$) we observe a positive $\bar{v}_n|_{r_I}$, which indicates that the jet is on average detrainning turbulent fluid. Thus, the local entrainment shows some coupling to the large-scale turbulence of the jet because it is the large-scale

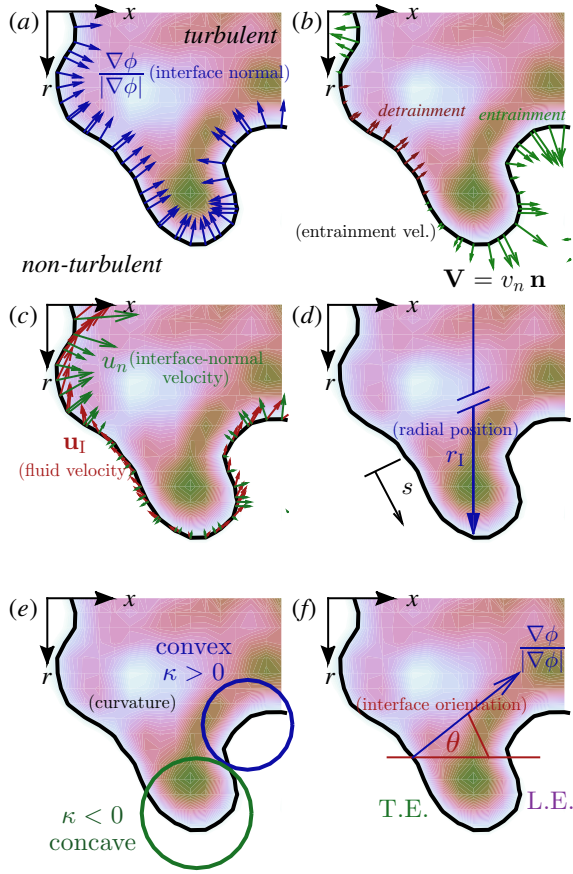


Figure 4. Definitions of variables pertaining to the TNTI. (a) Interface-normal unit vector \mathbf{n} . (b) Local entrainment velocity \mathbf{V} where positive entrainment is denoted by green vectors and detrainment is denoted by red vectors. (c) Local fluid velocity \mathbf{u}_f and interface-normal velocity u_n . (d) Radial distance to TNTI from jet centreline r_I . (e) Local surface curvature κ . (f) Interface orientation θ ; T.E. denotes the trailing edge and L.E. denotes the leading edge.

velocity fluctuations that transport the TNTI across radial positions that span several jet half-widths, $b_{u,1/2}$. Whereas the radial position of the TNTI results from large-scale flow features, the surface curvature of the TNTI tends to be formed by smaller scale structures that give rise to very sharp contortions (see figure 5b). The J-PDF of v_n and the local surface curvature is illustrated in figure 6(b). In agreement with the results of Wolf *et al.* (2013), there is greater entrainment when the curvature is positive (convex, see figure 4e) and greater detrainment when the curvature is negative (concave). The largest magnitudes of the entrainment velocity occur when the surface curvature is flat ($\kappa \approx 0$). However, when the interface is flat the distribution of v_n is nearly symmetric about $v_n = 0$ to give a conditional mean entrainment velocity that is negative (entraining) but small. This means there is only a weak preference for entrainment along flat regions of the TNTI.

As a function of interface orientation, figure 6(c) shows that there is preference for entrainment ($v_n < 0$) for $\theta > 0^\circ$. More specifically, there is greater entrainment along the leading edges of the TNTI ($\theta > 90^\circ$), in agreement with the trends reported by Watanabe *et al.* (2014) for DNS of a planar jet. The local entrainment behaviour is not significantly influenced by the interface orientation for $\theta < 0$

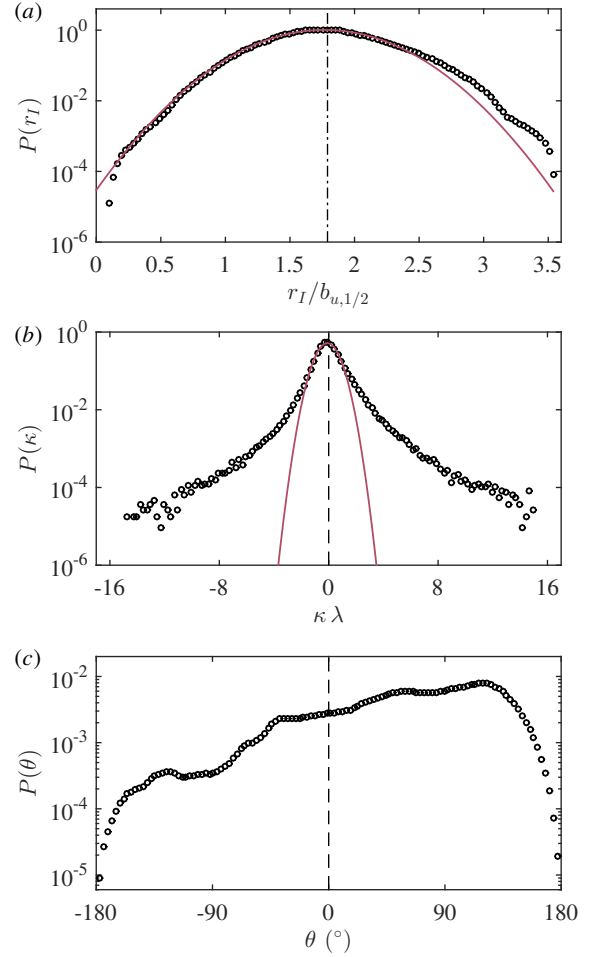


Figure 5. PDF of (a) the radial distance from the jet centreline to the TNTI r_I , (b) the local surface curvature defined by (3) κ and (c) the orientation of the TNTI. Gaussian profiles fitted to the distributions are denoted by the red lines.

because the v_n distributions are symmetric in this region to give $\overline{v_n}|\theta \approx 0$. In figure 6(c) we also present the conditional mean entrainment velocities that have also been conditioned on positive (convex) and negative (concave) curvatures. These profiles $\overline{v_n}|\theta|\kappa$ are illustrated as the purple dashed line for positive (convex) curvatures and the blue dash-dotted line for negative (concave) curvatures. The local entrainment along convex curvatures is not strongly dependent on the surface orientation because the conditional mean v_n remains relatively constant in the region $\theta > 0$. Along concave curvatures, there is greater entrainment along the leading edges of the TNTI $\theta > 90^\circ$, otherwise the conditional mean v_n is approximately zero or greater than zero (detraining) for all other angles.

FLOW-FIELD ABOUT THE TNTI

It is interesting to consider how the local flow field about the TNTI gives rise to the geometric features that are discussed above. This, in turn, will help establish a description of the kinematics of the flow that influences the local entrainment rates. We first evaluate the alignment between the local fluid velocity along the TNTI and the interface itself, as illustrated in figure 7(a). Here, the fluid velocity in a laboratory reference frame is represented by the grey vec-

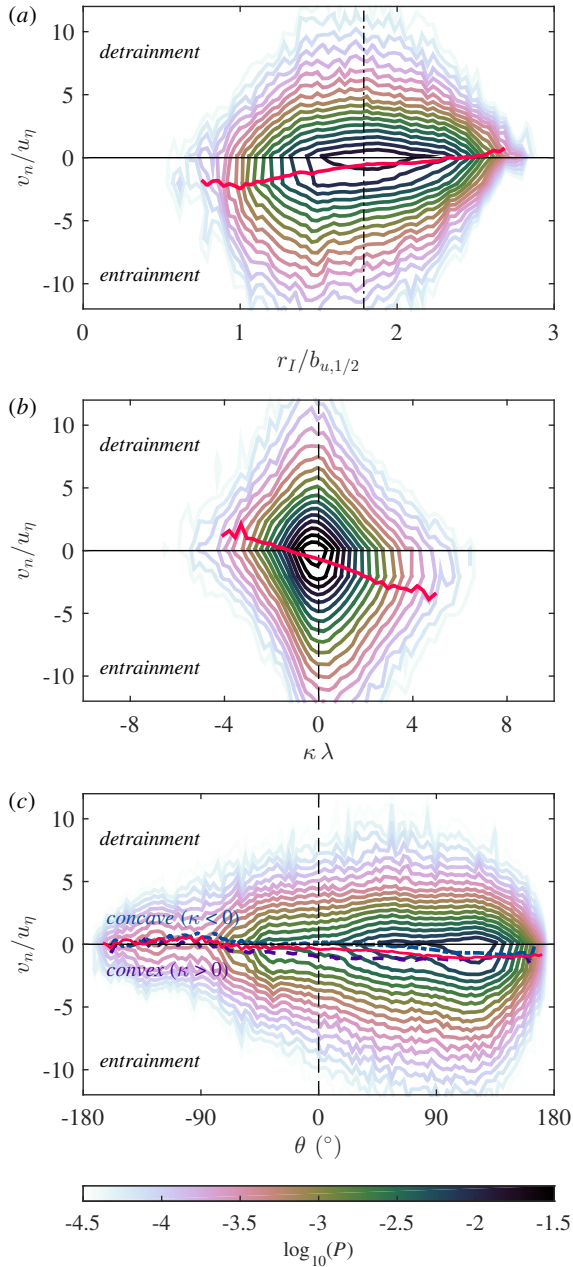


Figure 6. Joint-probability distribution functions of the entrainment velocity v_n as a function of (a) radial position r_I , (b) surface curvature κ and (c) interface orientation θ . The conditional mean entrainment velocity for a given value of the independent variable, $\overline{v_n}|_f$, is denoted by the red lines.

tors and the TNTI is denoted by the black line. We use a bi-linear interpolation scheme to interpolate the fluid velocity at each point along the TNTI, \mathbf{u}_I ; an example of this is denoted by the blue vector in figure 7(a). We then evaluate the alignment between \mathbf{u}_I and the local interface normal unit vector, \mathbf{n} , which is denoted by $\cos(\psi)$. A cosine value of 1 indicates that the local fluid velocity is aligned with the interface-normal and is advecting the TNTI towards the turbulent region. A cosine value of -1 indicates that the local fluid velocity is anti-aligned with the interface-normal and is advecting the TNTI away from the turbulent region. A cosine value of 0 indicates that the local fluid velocity is moving tangentially along the TNTI. The PDF of $\cos(\psi)$ is presented in figure 7(b), which demonstrates that there

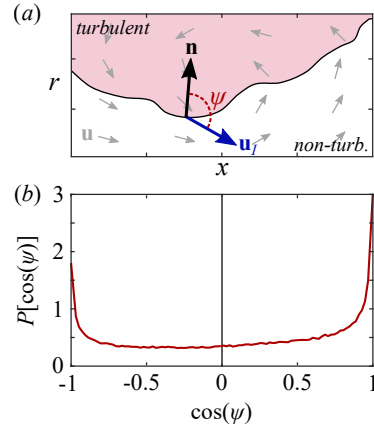


Figure 7. (a) Schematic illustrating $\cos(\psi)$, the alignment between the local fluid velocity \mathbf{u}_I and the interface-normal unit vector \mathbf{n} . (b) PDF of $\cos(\psi)$.

is strong preference for \mathbf{u}_I to be aligned ($\cos(\psi) = 1$) and anti-aligned ($\cos(\psi) = -1$) with the interface-normal \mathbf{n} .

Given the prevalence of fluid motion aligned normal to the TNTI, we now evaluate the characteristics of the interface-normal velocity, $u_n = \mathbf{u} \cdot \mathbf{n}$, in the region about the TNTI. This is achieved by conditionally-averaging the flow field along a coordinate that is locally-normal to the TNTI, which we denote as x_n . The origin of this coordinate is at the TNTI itself and the coordinate is positive towards the turbulent region. At each point along the coordinate we calculate the interface-normal velocity, which is then ensemble-averaged with data measured at the same distance from the TNTI for all realisations of the flow; these averaged quantities are denoted by $\langle \sim \rangle$. The black line in figure 8 represents the profile of the interface-normal velocity $\langle u_n \rangle$ about the TNTI. In the non-turbulent region ($x_n < 0$) the fluid is on average moving towards the TNTI ($u_n > 0$). In the turbulent region the fluid is on average moving towards the TNTI ($u_n < 0$), creating a counterflow profile about the interface. To gauge how the flow-field shapes the TNTI, we decompose $\langle u_n \rangle$ by further conditioning the profile based on the radial position r_I (a) and curvature κ (b). Each u_n profile conditioned on r_I and κ consist of an equal number of points (1/3 of total) along the TNTI (see inset plots in figure 8). We then ensemble average the profiles of $\langle u_n \rangle$ for each of the conditions for r_I and κ , which are colour-coded to match inset PDFs.

Figure 8(a) illustrates that there is a stronger inflow of non-turbulent fluid when the TNTI is closer to the jet centreline (see green line). In contrast, when the TNTI is in the outer region of the jet (*i.e.* far from the jet centreline, red) there is a much weaker inflow of non-turbulent fluid. Similar behaviour of the interface-normal velocity is illustrated for convex curvatures in figure 8(b), as shown by the green line. Here, there is greater inflow of non-turbulent fluid towards the turbulent jet along convex curvatures compared to concave curvatures. Thus, the geometric features that are coupled with entrainment (small r_I and convex curvature) are also linked to greater inflow of non-turbulent fluid. This behaviour also gives some indication that there are stronger pressure gradient forces present inside the turbulent region to induce greater inflow of non-turbulent fluid when the TNTI is near to the jet centreline and along convex curvatures. This inflow may be generated via the Biot-Savart law

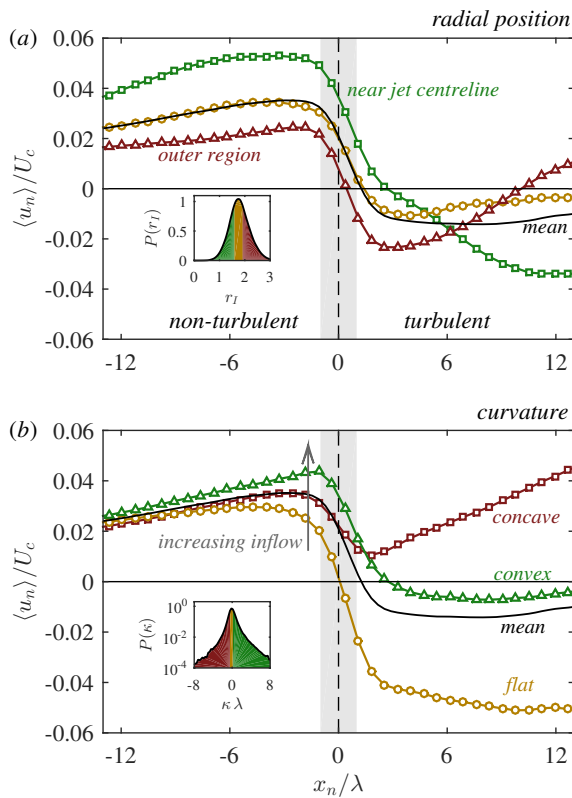


Figure 8. (a) Conditionally-averaged profile of the interface-normal velocity $\langle u_n \rangle$ along x_n with further conditioning based on the radial position of the TNTI. (b) Conditionally-averaged profile of the interface-normal velocity $\langle u_n \rangle$ along x_n with further conditioning based on the curvature of the TNTI. The inset plots illustrate the PDFs of (a) radial position and (b) curvature with the filled colours denoting the bins used for the conditional profiles.

by the large vortical structures that are characteristic of the TNTI in mean-shear flows da Silva *et al.* (2011), and these structures may play an important role in the local entrainment process.

SUMMARY AND CONCLUSIONS

In this paper we characterise the relationship between the local entrainment along the TNTI and geometric features of the interface in a turbulent jet. This is achieved by taking simultaneous, high-speed PIV and PLIF measurements in the far-field of a jet and implementing an interface-tracking technique. The geometric features we consider are the radial distance of the TNTI to the jet centreline, the surface curvature and the interface orientation. The distribution of the TNTI radial position indicates that there are large-scale velocity fluctuations of the jet that transport the TNTI over distances on the order of the jet half-width. This is contrasted by the distribution of surface curvatures, which indicate that the TNTI is also characterised by very small contortions. The entrainment velocity exhibits some dependence on the radial position and curvature on the TNTI, but is less dependent on orientation. Generally, there is greater entrainment when the TNTI is nearer to the jet centreline and along convex curvatures. We show that the local fluid advection velocity along the TNTI is preferentially aligned

and anti-aligned with the TNTI (*i.e.* normal to the interface). When the interface is near to the jet centreline and along convex curvatures there is greater inflow of fluid from the non-turbulent region to the turbulent region. This alludes to the presence of large vortical structures that generate greater inflow and influence the local entrainment rate along the TNTI.

Acknowledgements

The authors wish to thank the UK Engineering and Physical Sciences Research Council, the Norwegian Research Council and the Australian Research Council for the financial support of this work.

REFERENCES

- Borrell, G. & Jiménez, J. 2016 Properties of the turbulent/non-turbulent interface in boundary layers. *J. Fluid Mech.* **801**, 554–596.
- Chauhan, K., Philip, J., de Silva, C., Hutchins, N. & Marusic, I. 2014 The turbulent/non-turbulent interface and entrainment in a boundary layer. *J. Fluid Mech.* **742**, 119–151.
- Gampert, M., Boschung, J., Hennig, F., Gauding, M. & Peters, N. 2014 The vorticity versus the scalar criterion for the detection of the turbulent/non-turbulent interface. *J. Fluid Mech.* **750**, 578–596.
- Holzner, M. & Lüthi, B. 2011 Laminar superlayer at the turbulence boundary. *Phys. Rev. Lett.* **106**, 134503.
- Mistry, D., Philip, J., Dawson, J. R. & Marusic, I. 2016 Entrainment at multi-scales across the turbulent/non-turbulent interface in an axisymmetric jet. *J. Fluid Mech.* **802**, 690–725.
- Prasad, R. R. & Sreenivasan, K. R. 1989 Scalar interfaces in digital images of turbulent flows. *Exp. Fluids* **7**, 259–264.
- da Silva, C., dos Reis, R. & Pereira, J. 2011 The intense vorticity structures near the turbulent/non-turbulent interface in a jet. *J. Fluid Mech.* **685**, 165–190.
- de Silva, C. M., Philip, J., Chauhan, K., Meneveau, C. & Marusic, I. 2013 Multiscale geometry and scaling of the turbulent-nonturbulent interface in high Reynolds number boundary layers. *Phys. Rev. Letters* **111**, 044501.
- Watanabe, T., Sakai, Y., Nagata, K., Ito, Y. & Hayase, T. 2014 Enstrophy and passive scalar transport near the turbulent/non-turbulent interface in a turbulent planar jet flow. *Phys. Fluids* **26**, 105103.
- Watanabe, T., Sakai, Y., Nagata, K., Ito, Y. & Hayase, T. 2015 Turbulent mixing of passive scalar near turbulent and non-turbulent interface in mixing layers. *Phys. Fluids* **27**, 085109.
- Westerweel, J., Fukushima, C., Pedersen, J. & Hunt, J. C. R. 2009 Momentum and scalar transport at the turbulent/non-turbulent interface of a jet. *J. Fluid Mech.* **631**, 199–230.
- Wolf, M., Lüthi, B., Holzner, M., Krug, D., Kinzelbach, W. & Tsinober, A. 2012 Investigations on the local entrainment velocity in a turbulent jet. *Phys. Fluids* **24**, 105110.
- Wolf, M., Lüthi, B., Holzner, M., Krug, D., Kinzelbach, W. & Tsinober, A. 2013 Erratum: Investigations on the local entrainment velocity in a turbulent jet [Phys. Fluids 24, 105110 (2012)]. *Phys. Fluids* **25**, 019901.